Hydrol. Earth Syst. Sci. Discuss., 6, 2893–2929, 2009
www.hydrol-earth-syst-sci-discuss.net/6/2893/2009/

Hydrology and Earth System Sciences Discussions

Papers published in *Hydrology and Earth System Sciences Discussions* are under open-access review for the journal *Hydrology and Earth System Sciences*

Simulation and validation of subsurface lateral flow paths in an agricultural landscape

Q. Zhu and H. S. Lin

The Pennsylvania State University, Department of Crop and Soil Sciences, 116 Agricultural Sciences and Industry Building, University Park, PA 16802, USA

Received: 28 February 2009 – Accepted: 5 March 2009 – Published: 1 April 2009

Correspondence to: H. S. Lin (henrylin@psu.edu)

Published by Copernicus Publications on behalf of the European Geosciences Union.

Abstract

The importance of soil water flow paths to the transport of nutrients and contaminants has long been recognized. However, effective means of detecting subsurface flow paths in a large landscape is still lacking. The flow direction and accumulation algorithm in GIS hydrologic modeling is a cost effective way to simulate potential flow paths over a large area. This study tested this algorithm for simulating lateral flow paths at three interfaces in soil profiles in a 19.5-ha agricultural landscape in central Pennsylvania, USA. These interfaces were (1) the surface plowed layers (Ap1 and Ap2 horizons) interface, (2) the interface with subsoil clay layer where clay content increased to over 40%, and (3) soil-bedrock interface. The simulated flow paths were validated through soil hydrologic monitoring, geophysical surveys, and observable soil morphological features. The results confirmed that subsurface lateral flow occurred at the interfaces with the clay layer and the underlying bedrock. At these two interfaces, the soils on the simulated flow paths were closer to saturation and showed more temporally unstable moisture dynamics than those off the simulated flow paths. Apparent electrical conductivity in the soil on the simulated flow paths was elevated and temporally unstable as compared to those outside the simulated paths. The soil cores collected from the simulated flow paths showed significantly higher Mn contents at these interfaces than those away from the simulated paths. These results suggest that (1) the algorithm is useful in simulating possible subsurface lateral flow paths if used appropriately with sufficiently detailed digital elevation model; (2) repeated electromagnetic surveys can reflect the temporal change of soil water storage and thus is an indicator of soil water movement over the landscape; and (3) observable Mn content in soil profiles can be used as a simple indicator of water flow paths in soils and over the landscape.

1 Introduction

Contribution of subsurface lateral flow in soils to rapid transport of nutrients and chemicals has been well recognized (e.g., Tsukamoto and Ohta, 1988; Elliot et al., 1998). Therefore, generating three-dimensional (3-D) scheme of subsurface flow paths in a landscape can help nutrient management and pollution control. However, limited means are available for detecting (especially nondestructively) subsurface flow paths in a large landscape. In addition, most studies on subsurface lateral flow reported in the literature have been conducted in forested catchments (e.g., Kitahara et al., 1994; Sidle et al., 2001; Lin et al., 2006), with much fewer studies conducted in agricultural landscapes.

Soil-bedrock interface has been recognized in a number of recent studies as an important subsurface lateral flow path. For example, Freer et al. (1997) reported a positive correlation between total flow volume and the contributing area calculated from a digital elevation model (DEM) of the soil-bedrock interface (instead of the soil surface). Noguchi et al. (1999) demonstrated through dye tracing that bedrock topography was important in contributing to preferential flow in a forested hillslope. Buttle and McDonald (2002) found that water flow at bedrock surface occurred in a thin saturated layer. Haga et al. (2005) demonstrated that saturated subsurface flow above soil-bedrock interface was dominant subsurface runoff. Fiori et al. (2007) also reported that the principal mechanisms for the stream flow generation were subsurface flow along the soil-bedrock interface.

Because of often significant changes in texture, structure, or bulk density across the boundary of two adjacent soil horizons, soil horizon interface can also alter water flow directions and patterns (e.g., Kung, 1990, 1993; Ju and Kung, 1993; Gish et al., 2005). Several studies have reported water accumulation and subsequent lateral preferential flow above a high clay content and low hydraulic conductivity B horizon (called argillic horizon) (Haria et al., 1994; Perillo et al., 1999; Heppell et al., 2000). Slowly-permeable fragipans in many soils have also been recognized to develop seasonal perched water table and thus trigger lateral preferential flow (e.g., Palkovics and Peterson, 1977; McDaniel et al., 2008). Because of compaction caused by farming equipments, plowpan (Ap2 horizon) underneath plowed layer (Ap1 horizon) can also potentially generate lateral seepage especially in rice paddy soils (e.g., Chen et al., 2002; Sander and Gerke, 2007). Sidle et al. (2001) also observed lateral flow at organic horizon–mineral soil interface in forested hillslopes.

Although subsurface lateral flow at the interfaces between soil horizons and between soil and underlying bedrock are important to water flow and chemical transport across a landscape, methods for effectively determining where and when subsurface lateral flow occurs remain very limited. In recent years, the flow direction and accumulation simulations based on DEM have been implemented in Geographic Information System (GIS) hydrologic modeling tools (e.g., Maidment, 2002). These simulations are based on the deterministic 8 method (D8) single-flow algorithm (also called nondispersive algorithm) (O'Callaghan and Mark, 1984). Although the D8 method has been widely used in the simulation of surface flow paths (e.g., Marks et al., 1984; Jones, 2002; Schäuble et al., 2008), it has not been widely used to simulate subsurface flow paths. Gish et al. (2005) have used this modeling tool to identify subsurface lateral flow paths above the clay layer in an agricultural watershed, which were confirmed by ground-penetration radar (GPR) investigations. Bakhsh and Kanwar (2008) reported that flow accumulation generated from the D8 method contributed significantly to discriminate subsurface drainage clusters.

However, the D8 method only allows one of eight flow directions, which constrains the representation of flow path variability (Fairfield and Leymarie, 1991). Flow path simulated using the D8 tends to be concentrated to distinct, often artificially straight lines (Seibert and McGlynn, 2007). In addition, Kenny et al. (2008) pointed out that the D8 algorithm can not yield good simulation results in low relief areas or areas with poor DEMs. Efforts to alleviate these drawbacks have focused on introducing models with multiple-flow directions, also called dispersive algorithms. For example, the algorithm proposed by Quinn et al. (1991) (MD8) distributes flow to all neighboring downslope cells weighted according to slope. However, dispersive algorithms produce numerical dispersion from a DEM cell to all neighboring cells with a lower elevation, which may be inconsistent with the physical definition of upstream drainage area (Orlandini et al., 2003). Tarboton (1997) proposed a nondispersive algorithm (Dinf) that assigns flow direction angle between 0 and 2π radian and allows an infinite number of possible flow directions. However, a certain degree of dispersion still remains in this method (Orlandini et al., 2003). According to Paik (2008), dispersive algorithms cannot define specific flow paths, therefore they are not suitable for investigating the transport of nutrient, pollutant, and water through channel corridors. In this respect, nondispersive algorithms (e.g., D8) are preferable. A few studies have suggested that the D8 method can yield good results in areas of substantial relief using a high resolution DEM (e.g., 3–5 m resolution DEM) (Guo et al., 2004; Kenny et al., 2008; Paik, 2008; Wu et al., 2008).

The objective of this study was to investigate the reliability of DEM-derived flow direction and accumulation algorithm (D8) implemented in ArcGIS 9.2 (ESRI, Redlands, CA, USA) for simulating subsurface lateral flow paths at three interfaces in an agricultural landscape. The interfaces investigated included (1) the interface between the surface plowed layers of Ap1 and Ap2 horizons, (2) the interface with subsoil clay layer where clay content increased to over 40%, and (3) the interface between soil and the underlying bedrock. Three field indicators were then used to validate the simulated flow paths, including field soil moisture monitoring, electromagnetic induction (EMI) surveys, and soil manganese contents observed at these interfaces.

2 Materials and methods

2.1 Study site

This study was conducted in an agricultural landscape typical of the valley in the Northern Appalachian Ridges and Valleys physiographic region in the USA (Fig. 1). The

HESSD
6, 2893–2929, 2009

study area is located on The Pennsylvania State University's Kepler Farm in Rock Springs, PA, which has a delineated area of 19.5 ha. Typical crops grown on this farm are corn, soybean, and winter wheat. Elevation ranges from 373 m at the footslope in the northeastern corner to 396 m at the ridge top of the hill located in the middle portion of the field (Fig. 1). Depth to bedrock ranges from less than 0.25 m on the summit to more than 3 m on the footslope based on our field investigations. According to the second order soil survey (Soil Survey Division Staff, 1993), five soil series have been identified in this landscape: the Hagerstown, Opequon, Murrill, Nolin, and Melvin soil series (Fig. 1). There are some transition zones among these soil series on the soil map, including the Opequon-Hagerstown variant, Hagertown-Murrill variant, Hagerstown-Nolin variant, and Nolin-Melvin variant (Fig. 1). The dominant soil series are the Hagerstown silt loam (fine, mixed, semiactive, mesic Typic Hapludalfs) and the Opequon silty clay loam (clayey, mixed, active, mesic Lithic Hapludalfs). These are well-drained soils derived from limestone residuum, with the Hagerstown solum over 1.0 m thick and the Opequon solum <0.5 m thick. The Murrill series (fine-loamy, mixed, semiactive, mesic Typic Hapludults) consists of deep, well-drained soils formed in sandstone colluvium with underlying residuum weathered from limestone. The Melvin silt loam (fine-silty, mixed, active, nonacid, mesic Fluvaquentic Endoaquepts) and the Nolin silt loam (fine-silty, mixed, active, mesic Dystric Fluventic Eutrudepts) are deep soils formed in alluvium washed from surrounding uplands with limestone lying underneath the alluvium. The Nolin series is well-drained while the adjacent Melvin series is poorly-drained (closer to a nearby stream).

2.2 Subsurface flow paths simulation

The DEMs of the three interfaces (the Ap1 to Ap2 interface, the interface with the clay layer, and the soil-bedrock interface) were generated by subtracting the land surface DEM (3-m resolution) by the Ap1 horizon thickness, depth to clay layer, and depth to bedrock, respectively. Depth to clay layer was defined as the depth to the first horizon with more than 40% clay. For the Nolin and Melvin series, the horizon with >40% clay was not observed (27–29% clay in their B horizons); however, a restrictive horizon with greater density (>1.6 g/cm^3) was presented at the depth range of 0.6–1.0 m. For simplicity, we used the depth to this restrictive horizon in the Nolin and Melvin soils to approximate their depth to clay layer since these two soil series only occupied a small portion of the overall landscape.

Ordinary kriging was used to generate the maps of the Ap1 horizon thickness from 145 soil cores collected from the study area, and the depth to clay layer map was generated from 70 of these soil cores (see Fig. 1 for the spatial locations of these soil cores). Regression kriging was used to interpolate the depth to bedrock from 77 point observations (Fig. 1). The selection of different spatial interpolation methods was based on a combined consideration of spatial structure and auxiliary variables (Zhu and Lin, 2009), i.e., soil properties with a small ratio of sample spacing over spatial correlation range (<0.5) should be interpolated with ordinary kriging, while soil properties with strong correlation with auxiliary variables (R^2>0.6) are better interpolated with regression kriging. All spatial interpolations in this study were implemented using the ArcGIS Geostatistical Analyst.

Potential lateral flow paths at the interfaces of Ap1–Ap2, clay layer, and soil-bedrock were simulated using the flow direction and accumulation algorithm implemented in the ArcGIS 9.2 hydrologic modeling tool. The flow direction provides a grid of flow directions from one cell to its steepest downslope using the D8 single-flow algorithm (see illustration in Fig. 2). The flow accumulation determines the accumulated water from all cells in contributing area that flow into each downslope cell. Wu et al. (2008), via comparing different DEM resolutions (10, 30, 60, 90, 150, and 200 m), found that higher DEM resolution led to more accurate D8 simulation. The 3-m resolution DEM used in this study is better than many previous studies reported in the literature (e.g., 5- and 10-m resolution DEMs in the studies of Erskine et al., 2006, and Thompson et al., 2006, respectively).

A threshold of contributing area was used to determine whether a cell was involved in a flow path. A smaller threshold indicates more cells participating in the flow. Thus, a smaller threshold is better to simulate flow paths under wet condition, while a larger threshold is better suited for dry condition. To date, no definitive model has emerged that provides clear criteria for selecting such a threshold value. Besides, flow initiation mechanisms are likely to vary depending on local characteristics of climate, geology, soils, relief, and vegetation (e.g., Kirkby, 1994; Vogt et al., 2003). In the study of Gish et al. (2002), a threshold of 100 m^2 was suggested, while in the study of Bakhsh and Kanwar (2008) a threshold of 420 m^2 was used. In our study, instead of using a single threshold, we compared three thresholds of contributing area: 1000, 500 and 100 m^2. The output from each flow simulation in the ArcGIS was a raster file, which was converted to a vector file for generating three buffer zones of 0–5, 5–10, and 10–15 m away from the simulated flow paths in order to compare with the EMI survey data.

After flow path simulations, 145 monitoring sites were superimposed to determine whether a site was on or off the simulated flow paths (Fig. 3). If a monitoring site was in the cell of the simulated flow path or in the cell adjacent to the simulated path, it was considered as on the flow path; otherwise, it was considered as off the flow path (Fig. 2). Since our DEM cell size was 3×3 m, if the maximal distance from a monitoring site to the simulated flow paths was less than 4.5 or 6.3 m (depending on orientation) (see Fig. 2), then this site was considered to be on the flow path. Gish et al. (2005) used a similar criteria (<5 m away from the simulated flow path) to determine whether a cell was on or off predicted lateral flow paths.

2.3 Data collections for validating simulated flow paths

Three sets of data were collected in the field to validate the simulated flow paths. These field data were: (1) soil moisture monitoring (including volumetric soil water content and matric potential), (2) EMI surveys, and (3) observable soil manganese (Mn) content at the three interfaces.

Soil water content at multiple depths was monitored at 145 locations distributed throughout the farm (Fig. 1). Our procedure followed that used by Lin et al. (2006). Briefly, a portable TRIME-FM Time Domain Reflectomery (TDR) Tube Probe (IMKO, Ettlingen, Germany) was used to determine volumetric soil water content while being placed at specific depth interval in a PVC access tube installed at each site. These 145 sites covered all of the landforms and soil series in the study area (Table 1). At each site, readings were taken at six depth intervals of 0–0.1, 0.1–0.3, 0.3–0.5, 0.5–0.7, 0.7–0.9, and 0.9–1.1 m (representing soil water content at 0.1, 0.2, 0.4, 0.6, 0.8, and 1.0 m depth, respectively). If the depth to bedrock at a monitoring site was not sufficiently deep to allow all six depth measurements, fewer readings were taken. The actual number of subsoil moisture observations was 110 and 96 for the 0.3–0.5 m and 0.7–0.9 m depth intervals, respectively. Whole farm soil water contents at all of these 145 locations were collected for 12 times from 2005 to 2007 (Table 2).

Seventy-four out of these 145 monitoring sites were also selected for tensiometer installation (Fig. 1). These 74 locations were selected based on landforms and soil series in the study area (Table 1). Nested tensiometers were installed at five depths of 0.1, 0.2, 0.4, 0.8, and 1.0 m at each of these 74 sites. They were 0.15 m away from the TDR access tubes. Soil matric potential along with soil water content at these 74 locations were measured for 14 times from 2006 to 2008 (Table 2).

A 1.1-m long intact soil core (0.038-m in diameter) was collected from each of the 145 soil moisture monitoring sites during the time when we installed the TDR access tubes. Seventy out of these 145 soil cores were selected for basic analysis and profile description, including particle size distribution and Mn mottle content in each horizon (including that at the three interfaces). Particle size distribution was analyzed using the method proposed by Kettler et al. (2001). The Mn content was estimated visually following the standard procedure described in Soil Survey Manual for redox amount estimation (Soil Survey Division Staff, 1993).

Apparent electrical conductivity (ECa) values were collected with EM38 sensor (Geonics, Mississauga, Canada) on four dates of 16 January, 10 March, 30 April, and 4 June 2008. The EM38 sensor operated at a frequency of 13.2 KHz and provided effective theoretical measurement depths of 1.5 m when operated in vertical dipole mode. These EMI surveys were conducted with the same spatial resolution of about 3×8 m

HESSD
6, 2893–2929, 2009

(3-m spacing between two consecutive readings and 8-m apart traverse lines across the farm). The readings in the EMI surveys are affected by soil properties such as clay content, moisture content, organic matter content, salinity, and depth to bedrock (Rhoades et al., 1976; Auerswald et al., 2001; Corwin and Lesch, 2005). We assumed that only soil moisture was changed during the period of our EMI surveys from January to June 2008 while other soil properties remained pretty much unchanged. Although temperature was also a changing factor, all EMI readings were corrected to a standard temperature of 25°C. Ordinary kriging was used to generate the EMI maps for the entire study area based on its spatial structure (Zhu and Lin, 2009).

2.4 Data analysis

For the 74 sites with both soil water content and matric potential monitoring, soil water retention curves (SWRC) at different depths in each site were fitted with the model of van Genuchten (1980):

$$\frac{\theta(h)-\theta_r}{\theta_s-\theta_r}=\left[\frac{1}{1+(\alpha h)^n}\right]^{(n-1)/n}, \tag{1}$$

where α and n are empirical parameters; θ_s and θ_r are saturation and residual water contents, respectively; h is matric potential and $\theta(h)$ is volumetric water content under h. Examples of fitted SWRC for typical soil series, texture classes, and horizons in the study area are shown in Fig. 4. Texture class was one of the main factors affecting the shape of the SWRC. For example, in the Ap horizon, as the texture class changed from silty clay loam to silt loam, θ_s decreased from 0.43 to 0.37 $m^3 m^{-3}$ (Fig. 4a, d, g). For the same texture class (e.g., silt loam) and soil series (e.g., Murrill), θ_s decreased from 0.37 to 0.32 $m^3 m^{-3}$ as the soil horizon changed from Ap to Bt2 (Fig. 4g, h, i). Because of plowing and root growth, surface soils had lower bulk density, more pore space, and thus greater θ_s than subsurface soils.

Volumetric soil water contents at the field capacity (0.33 kPa) and saturation (0 kPa) for each depth and each site were estimated through the fitted curve. The estimated

HESSD

6, 2893–2929, 2009

Subsurface lateral flow paths in an agricultural landscape

Q. Zhu and H. S. Lin

water contents at the field capacity ranged from 0.2 to 0.3 $m^3 m^{-3}$, while the estimated water contents at saturation ranged from 0.35 to 0.45 $m^3 m^{-3}$ for the entire study area. The ratio of field capacity over saturation ranged from 0.60–0.65 (with a mean of 0.63). These estimated soil water contents at field capacity and saturation of all depths and all 74 sites were grouped according to their soil horizons (Ap, Bt1, and Bt2) and texture classes (silt loam, silty clay loam, and silty clay) (Fig. 5). The difference between Ap1 and Ap2 horizons was not considered here for two reasons: (1) the Ap1 horizon varied in thickness from 0.08 to 0.13-m in the study area; therefore, tensiometers installed at 0.1-m depth were located in the transition zones of Ap1 to Ap2 horizons; and (2) the TRIME-FM TDR probe was 0.18-m in length, thus soil water content of the Ap1 (0–0.1 m below the ground surface) and Ap2 (0.1–0.3 m below the ground surface) could not be clearly separated. Although the Ap2 horizon was denser than the Ap1 horizon, such density contrast was less strong as compared to that between Ap and Bt horizons in the study area.

For volumetric soil water content collected at each specific depth of each monitoring site, relative degree of saturation (*RS*) was calculated by dividing it by the estimated saturated water content of this horizon and texture class (Fig. 5). A *RS* close to 1 suggests near saturation. At a specific soil horizon interface, 95% confidence intervals for the *RS* values between sites on and off the simulated flow paths were calculated using SAS (SAS Institute Inc., Cary, NC, USA). These confidence intervals were then compared using one-way ANOVA to determine whether significant differences in the *RS* existed between sites on and off the simulated flow paths. Similarly, 95% confidence intervals of the *RS* values at, below, and above a specific interface (Ap1–Ap2, clay layer, or soil-bedrock) were also compared to determine whether significant differences existed.

At each interface, temporal stability of the *RS* values of all 145 monitoring sites was analyzed using the approach proposed by Vachaud et al. (1985):

$$R_j = \frac{1}{N}\sum_{i=1}^{N} R_{ij}, \tag{2}$$

$$\delta_i = \frac{1}{M}\sum_{j=1}^{M}\left(\frac{R_{ij} - R_j}{R_j}\right), \tag{3}$$

$$S_\delta = \sqrt{\frac{1}{M}\sum_{j=1}^{M}\left(\delta_{ij} - \delta_i\right)^2}, \tag{4}$$

where R_j is the arithmetic mean of *RS* at all sites in day j; R_{ij} is the *RS* of a particular interface at site i in day j; N is the number of monitoring sites (in this study, N=145); δ_i is the arithmetic mean of the relative difference of *RS* at site i; M is the number of times that the whole farm soil water content was measured (in this study, M=12); and S_δ is the standard deviation of δ_i. Positive or negative δ_i suggests that at a particular interface, site i is wetter (positive δ_i) or dryer (negative δ_i) than the average condition of the entire farm. The S_δ depicts the magnitude of temporal stability of *RS* at a particular interface at site i. Higher S_δ value indicates a more dynamic change (i.e., temporally unstable) in soil moisture.

Following the same procedure, we conducted the temporal stability analysis of ECa values collected in four EMI surveys. Temporal stability of ECa in the three buffer zones (0–5, 5–10, and 10–15 m away from the simulated flow paths) and the rest of the study area were statistically compared with each other through t-test in SAS ($p<0.05$). The temporal changes in ECa reflected the change in soil water content. Therefore, the magnitude of ECa temporal stability can represent the degree of change in soil water storage in the three buffer zones of the predicted flow paths vs. the rest of the study area.

At the three interfaces studied, Mn contents estimated from soil cores were also statistically compared between sites on and off the simulated paths through t-test in SAS ($p<0.05$). The Mn mass observed in soil is an indicator of soil water movement as demonstrated in other studies (e.g., McDaniel et al., 2008; Walker and Lin, 2008). This is because Mn can be easily reduced and mobilized with moving water, and then oxidized and re-deposited when soil dries and O_2 reenters the soil (Patrick and Henderson, 1981). Therefore, high Mn concentration often indicates water flow paths.

3 Results and discussions

3.1 Simulated subsurface lateral flow paths

The spatial patterns of potential lateral flow paths at the three interfaces simulated with different thresholds of contributing area (i.e., 100, 500, and 1000 m^2) are illustrated in Fig. 3, where the patterns using the thresholds of 1000 and 500 m^2 were close to each other but quite different from that using the threshold of 100 m^2. Because of the topography of the study area, very few locations (<8% of the entire area) had a contribution area >500 m^2. Therefore, the simulated flow paths using the threshold contribution areas of 1000 and 500 m^2 were sparse and similar. In comparison, 25% cells of the entire study area had contribution area >100 m^2. In the subsequent analysis, we focus on comparing the simulated flow paths obtained with 500 and 100 m^2 thresholds.

In Fig. 3, water moved laterally out of the landscape through the soil-bedrock interface in three main areas: the north-east corner, the mid-west depressional area, and the mid-south portion. When using a smaller threshold (100 m^2), more areas participated in the flow paths, leading to 61% of the soil water monitoring sites (total 88 sites) being identified as on the simulated flow paths (Fig. 3c). In contrast, during drier condition using a larger threshold of 500 m^2, only 35% of the 145 monitoring sites were identified as on the simulated flow paths (Fig. 3b).

In the study area, the maximum difference in land surface elevation was 23 m between the lowest point in footslope and the highest point in ridge top. However, the largest differences of the Ap1 horizon thickness and depths to clay layer and bedrock in the entire landscape were less than 2 m (i.e., <8.7% of the surface elevation change). Consequently, the topography of the three interfaces was dominated by the variation in land surface elevation, resulting in nearly identical spatial patterns in the simulated lateral flow paths among the three interfaces. In the study of Birkhead et al. (1996), the bedrock topography derived from GPR image was also shown to be closely related to the surface topography (elevations of bedrock and ground surface decreased simultaneously for about 1.5 m in a 90-m transect).

3.2 Validating the simulated flow paths through soil hydrologic monitoring

At each of the three interfaces, the *RS* values between the monitoring sites on and off the simulated flow paths were statistically compared. In relative dry condition (average volumetric soil water content $\bar{\theta}$ at the clay layer and soil-bedrock interfaces were smaller than 0.28 and 0.31 $m^3 m^{-3}$, respectively), the *RS* values of the sites on the simulated flow paths (500 m^2 threshold) were significantly greater ($p<0.05$) than those sites off the paths at both the clay layer and soil-bedrock interfaces (Fig. 6b, c), but not at the Ap1–Ap2 interface (Fig. 6a). During the relative dry period, more drainage areas were required to initiate the lateral subsurface flow upon rainfall inputs. Thus, a greater threshold (e.g., 500 m^2) simulated better the potential lateral flow paths.

In relative wet condition ($\bar{\theta}>0.28$ and 0.31 $m^3 m^{-3}$ at the clay layer and soil-bedrock interfaces, respectively), significant difference ($p<0.05$) in the *RS* values also existed between the sites on and off the simulated flow paths (100 m^2 threshold) at both the clay layer and soil-bedrock interfaces (Fig. 6b, c), but, again, not at the Ap1–Ap2 interface (Fig. 6a). In our study area, the soil water content generally increased with depth and often reached the highest value at the soil-bedrock interface (see Fig. 8 illustrating typical soil moisture profile in each of the five soil series). Even during relatively dry period, the soil at the soil-bedrock interface might still be wet and free water lateral movement could occur after large rainstorms. In such case, a smaller threshold of 100 m^2 could also reasonably simulate lateral subsurface flow paths at the soil-bedrock interface. This is supported by some significant differences in soil moisture between the sites on and off the flow paths in Fig. 6c.

Unlike the *RS* values at the clay layer and soil-bedrock interfaces, no significant difference in the *RS* values was observed between the sites on and off the simulated flow paths at the Ap1–Ap2 interface (Fig. 6a). When describing soil cores, many macrospores (earthworm holes and root channels) were observed in connecting the Ap1 and Ap2 horizons. These macrospores could have transported water from the Ap1 to Ap2 horizon without much restriction and thus prevented the water from accumulating at the Ap1–Ap2 interface. In contrast, the clay layer interface was generally deeper than 0.4 m in the study area. At such depth, fewer roots and worm holes were observed and thus the vertical water percolation could be restricted.

To further verify the water accumulation at the clay layer interface, the *RS* values at this interface were statistically compared with the *RS* values right below this interface and 0.2-m above this interface (Fig. 7a). In relative dry condition ($\bar{\theta}$ <0.28 $m^3 m^{-3}$), the *RS* values at this interface for the sites on the simulated flow paths (500 m^2 threshold) were significantly greater (p<0.05) than that above and below it. In relative wet condition ($\bar{\theta}$ >0.28 $m^3 m^{-3}$), such significant difference (p<0.05) in the *RS* values also existed between the sites on and off the flow paths simulated with the threshold of 100 m^2. For the sites off the simulated flow paths, differences in the *RS* values between the clay layer interface and that above or below it were not significant in either dry or wet conditions (Fig. 7a).

For the sites on the flow paths simulated with the threshold 100 m^2, the *RS* values at the soil-bedrock interface were significantly greater (p<0.05) than those 0.2-m above it, regardless of the wetness condition (Fig. 7b). In comparison, for sites on the flow paths simulated with the threshold 500 m^2, significant difference in the *RS* values between the soil-bedrock interface and 0.2-m above the interface could only be observed in relatively dry condition ($\bar{\theta}$ <0.31 $m^3 m^{-3}$). This further suggests that a smaller threshold (100 m^2) works better to simulate flow paths at the soil-bedrock interface in both dry and wet conditions.

The temporal stability of the *RS* values between the sites on and off the simulated flow paths (100 m^2) at all three interfaces were compared in Fig. 9. At the clay layer and soil-bedrock interfaces, sites on the simulated flow paths had greater relative differences of *RS* and standard deviations than the sites off the paths (Fig. 9b, c), suggesting a more dynamic (and thus unstable) moisture status over time for the sites on the flow paths. At the clay layer interface, 70% of the sites on the flow paths had δ_i>0 and 75% of them had standard deviation of δ_i>0.1, while only 13% and 36% of the sites off the flow paths had δ_i>0 and standard deviation of δ_i>0.1, respectively. At the soil-bedrock layer interface, percentages of the sites on the flow paths with positive δ_i value and high standard deviation (>0.1) were even greater, 85% and 90%, respectively, while the corresponding percentages were only 12% and 36% for the sites off the flow paths. This observation indicates that the clay layer and soil-bedrock interfaces at the sites on the simulated flow paths were largely wetter and more temporally unstable, implying more water movement through these interfaces in general. De Lannoy et al. (2006) also documented that subsurface lateral flow resulted in high temporal variability of soil water content at the clay layer interface. At the Ap1–Ap2 interface, the sites on and off the simulated flow paths had no distinct differences in δ_i (Fig. 9a). When flow paths threshold (100 m^2) in Fig. 9 was changed to 500 m^2, similar results were observed (data not shown).

3.3 Validating the simulated flow paths through repeated EMI surveys

The temporal stability of ECa values in different buffer zones of the simulated flow paths is shown in Fig. 10 with a threshold of 500 m^2. As the distance from the simulated flow paths increased, both the mean and standard deviation of the relative difference in ECa decreased, suggesting that the soils closer to the simulated flow paths tended to have elevated and more dynamic ECa values. Additionally, the positive relative differences in ECa in the three buffer zones (0–5, 5–10, and 10–15 m) imply that their ECa values were greater than the overall average of the entire landscape. Their greater standard deviations further suggest that the soil ECa values in areas closer to the simulated flow paths had higher temporal variations than the soil further away from these paths (Fig. 10).

Previous studies have used soil ECa values to represent soil water content. Sherlock and McDonnell (2003) reported that soil ECa measurements using EM38 vertical dipole mode could explain over 70% of gravimetrically determined soil-water variance. Reedy and Scanlon (2003) also used the same sensor to explain 80% of the averaged volumetric water content in the soil profile. We assumed that the change in soil water content was the main control of the temporal variation in ECa values during our repeated EMI surveys from January to June 2008 (note that all temperatures were corrected to a standard value). Therefore, the higher and more unstable soil ECa values in areas closer to the simulated flow paths suggest increased wetness and more dynamic moisture changes.

3.4 Validating the simulated flow paths through soil morphological features

The simulated flow paths were further validated through the spatial variation in soil Mn contents at the clay layer and soil-bedrock interfaces (Fig. 11). For the sites on the simulated flow paths (threshold of 500 m^2), soils Mn content at these interfaces were generally greater than 1% and reached as high as 5–10% at some locations. However, for the sites off the simulated flow paths, almost no Mn was observed at these two interfaces. Other studies have suggested that soil Mn content is a good indicator of water movement in soil profiles. For example, Yaalon et al. (1977) found that soil Mn content was topography and drainage related in three catenas. McDaniel and Buol (1991) and Walker and Lin (2008) reported greater soil Mn content at footslope and concave landscape positions because of water accumulation. Cassel et al. (2002) reported relationship between subsurface flow paths and dissolved Mn from higher to lower elevations on hillslopes. Therefore, locations with greater soil Mn content are expected to be on or closer to subsurface flow paths.

4 Conclusions

Through validation by soil hydrologic monitoring, EMI surveys, and soil morphological observations, it was apparent that subsurface lateral flow occurred at the interfaces with the clay layer (or water-restrictive layer) and the underlying bedrock in the agricultural landscape, but not at the interface between surface plowed layers of the Ap1 and Ap2 horizons. The ArcGIS hydrologic modeling (the D8 algorithm) did a reasonable job in simulating potential lateral flow paths at these interfaces. Such simulated subsurface lateral flow paths, however, were temporally dynamic as they varied with the wetness condition of the landscape. Hence, using different thresholds of contributing area for the GIS hydrologic simulation would be needed to obtain expected results under different moisture conditions (e.g., 500 m^2 for relatively dry condition and 100 m^2 for relatively wet condition in this study). Sufficiently detailed DEM is also needed to ensure that the GIS flow algorithm performs with lower uncertainty. We suggest additional testing of this cost-effective means of predicting likely subsurface flow paths in other landscapes in order to establish a solid protocol for simulating subsurface hydrologic flow paths in different watersheds. Repeated EMI surveys could also provide another low-cost and nondestructive means of detecting potential subsurface flow paths.

Acknowledgements. This research was partially supported by the USDA Higher Education Challenge Competitive Grants Program (Grant no. 2006-38411-17202).

References

Auerswald, K., Simon, S., and Stanjek, H.: Influence of soil properties on electrical conductivity under humid water regimes, Soil. Sci., 166, 382–390, 2001.

Bakhsh, A. and Kanwar, R. S.: Soil and landscape attributes interpret subsurface drainage clusters, Aust. J. Soil. Res., 46, 735–744, 2008.
Birkhead, A. L., Heritage, G. L., White, H., and van Niekerk, A. W.: Ground-penetrating radar as a tool for mapping the phreatic surface, bedrock profile, and alluvial stratigraphy in the Sabie River, Kruger National Park, J. Soil Water Cons., 51, 234–241, 1996.
Burns, D. A., Hooper, R. P., McDonnell, J. J., Freer, J. E., Kendall, C., and Beven, K.: Base cation concentrations in subsurface flow from a forested hillslope: The role of flushing frequency, Water Resour. Res., 34, 3535–3544, 1998.
Buttle, J. M. and McDonald, D. J.: Coupled vertical and lateral preferential flow on a forested slope, Water Resour. Res., 38, 1060, doi:10.1029/2001WR000773, 2002.
Cassel, D. K., Afyuni, M. M., and Robarge, W. P.: Manganese distribution and patterns of soil wetting and depletion in a piedmont hillslope, Soil Sci. Soc. Am. J., 66, 939–947, 2002.
Chen, S. K., Liu, C. W., and Huang, H. C.: Analysis of water movement in paddy rice fields (II) simulation studies, J. Hydrol., 268, 259–271, 2002.
Corwin, D. L. and Lesch, S. M.: Apparent soil electrical conductivity measurements in agriculture, Comput. Electron. Agr., 46, 11–43, 2005.
De Lannoy, G. J. M., Verhoest, N. E. C., Houser, P. R., Gish, T. J., and van Meirvenne, M.: Spatial and temporal characteristics of soil moisture in an intensively monitored agricultural field (OPE3), J. Hydrol., 331, 719–730, 2006.
Elliot, J. A., Cessna, A. J., Best, K. B., Nicholaichuk, W., and Tollefson, L. C.: Leaching and preferential flow of clopyralid under irrigation: field observations and simulation modeling, J. Environ. Qual., 27, 124–131, 1998.
Erskine, R. H., Green, T. R., Ramirez, J. A., and MacDonald, L. H.: Comparison of grid-based algorithms for computing upslope contributing area, Water Resour. Res., 42, W09416, doi:10.1029/2005WR004648, 2006.
Fairfield, J. and Leymarie, P.: Drainage networks from grid digital elevation models, Water Resour. Res., 27, 709–717, 1991.
Fiori, A., Romanelli, M., Cavalli, D. J., and Russo, D.: Numerical experiments of streamflow generation in steep catchments, J. Hydrol., 339, 183–192, 2007.
Freer, J., McDonnell, J., Beven, K. J., Brammer, D., Burns, D., Hooper, R. P., and Kendall, C.: Topographic controls on subsurface storm flow at the hillslope-scale for two hydrologically distinct small catchments, Hydrol. Processes, 11, 1347–1352, 1997.
Gish, T. J., Dulaney, W. P., Kung, K.-J. S., Daughtry , C. S. T., Doolittle, J. A., and Miller, P.

T.: Evaluating use of ground-penetrating radar for identifying subsurface flow pathways, Soil Sci. Soc. Am. J., 66, 1620–1629, 2002.
Gish, T. J., Walthall, C. L., Daughtry, C. S. T., and Kung, K.-J. S.: Using soil moisture and spatial yield patterns to identify subsurface flow pathways, J. Environ. Qual., 34, 274–286, 2005.
Guo, J. H., Liang, X., and Leung, L. R.: A new multiscale flow network generation scheme for land surface models, Geophys. Res. Lett., 32, L23502, doi:10.1029/2004GL021381, 2004.
Haga, H., Matsumoto, Y., Matsutani, J., Fujita, M., Nishida, K., and Sakamoto, Y.: Flow paths, rainfall properties, and antecedent soil moisture controlling lags to peak discharge in a granitic unchanneled catchment, Water Resour. Res., 41, W12410, doi:10.1029/2005WR004236, 2005.
Haria, A. H., Johnson, A. C., Bell, J. P., and Batchelor, C. H.: Water-movement and isoproturon behaviour in a drained heavy clay soil. 1. Preferential flow processes, J. Hydrol., 163, 201–216, 1994.
Heppell, C. M., Burt, T. P., and Williams, R. J.: Variations in the hydrology of an underdrained clay hillslope, J. Hydrol., 227, 236–256, 2000.
Jones, R.: Algorithms for using a DEM for mapping catchment areas of stream sediment samples, Comput. Geosci., 28, 1051–1060, 2002.
Ju, S. H. and Kung, K.-J. S.: Finite element simulation of funnel flow and overall flow property induced by multiple soil layers, J. Environ. Qual., 22, 432–442, 1993.
Kenny, F., Matthews, B., and Todd, K.: Routing overland flow through sinks and flats in the interpolated raster terrain surfaces, Comput. Geosci., 34, 1417–1430, 2008.
Kettler, T. A., Doran, J. W., and Gilbert, T. L.: Simplified method for soil particle-size determination to accompany soil-quality analyses, Soil Sci. Soc. Am. J., 65, 849–852, 2001.
Kirkby, M. J.: Thresholds and instability in stream head hollows: a model of magnitude and frequency for wash processes, in: Process Models and Theoretical Geomorphology, edited by: Kirkby, M. J., Wiley, Chichester, 295–314, 1994.
Kitahara, H,, Terajima, T., and Nakai, Y.: Ratio of pipe flow to throughflow discharge, J. Jpn. Forest. Soc., 76, 10–17, 1994.
Kung, K.-J. S.: Preferential flow in a sandy vadose zone: 1. Field observation, Geoderma, 46, 51–71, 1990.
Kung, K.-J. S.: Laboratory observation of the funnel flow mechanism and its influence on solute transport, J. Environ. Qual., 22, 91–102, 1993.
Lin, H. S., Kogelmann, W., Walker, C., and Bruns, M. A.: Soil moisture patterns in a forested

catchment: A hydropedological perspective, Geoderma, 131, 345–368, 2006.
Maidment, D.: Arc Hydro: GIS for Water Resources, ESRI, Redlands, CA, USA, 2002.
Marks, D., Dozier, J., and Frew, J.: Automated basin delineation from digital elevation data, GeoProcessing, 2, 299–311, 1984.
McDaniel, P. A. and Buol, S. W.: Manganese distributions in acid soils of the North Carolina Piedmont, Soil Sci. Soc. Am. J., 55, 152–158, 1991.
McDaniel, P. A., Regan, M. P., Brooks, E., Boll, J., Bamdt, S., Falen, A., Young, S. K., and Hammel, J. E.: Linking fragipans, perched water tables, and catchment-scale hydrological processes, Catena, 73, 166–173, 2008.
Noguchi, S., Tsuboyama, Y., Sidle, R. C., and Hosoda, I.: Morphological characteristics of macropores and the distribution of preferential flow paths in a forested slope segment, Soil Sci. Soc. Am. J., 63, 1413–1423, 1999.
O'Callaghan, J. F. and Mark, D. M.: The extraction of drainage networks from digital elevation data, CVGIP, 28, 323–344, 1984.
Orlandini, S., Moretti, G., Franchini, M., Aldighieri, B., and Testa, B.: Path-based methods for the determination of nondispersive drainage directions in grid-based digital elevation models, Water Resour. Res., 39, 1144, doi:10.1029/2002WR001639, 2003.
Paik, K.: Global search algorithm for nondispersive flow path extraction, J. Geophys. Res., 113, F04001, doi:10.1029/2007JF000964, 2008.
Palkovics, W. E. and Petersen, G. W.: Contribution of lateral soil-water movement above a fragipan to streamflow, Soil Sci. Soc. Am. J., 41, 394–400, 1977.
Patrick, W. H. and Henderson, R. E.: Reduction and reoxidation cycles of Manganese and Iron in flooded soil and in water solution, Soil Sci. Soc. Am. J., 45, 855–859, 1981.
Perillo, C. A., Gupta, S. C, and Moncrief, J. F.: Prevalence and initiation of preferential flow paths in a sandy loam with argillic horizon, Geoderma, 89, 307–331, 1999.
Quinn, P. F., Beven, K. J., Chevallier, P., and Planchon, O.: The prediction of hillslope flowpaths for distributed modelling using digital terrain models, Hydrol. Processes, 5, 59–80, 1991.
Reedy, R. C. and Scanlon, B. R.: Soil water content monitoring using electromagnetic induction, J. Geotech. Geoenviron. Eng., 129, 1028–1039, 2003.
Rhoades, J. D., Raats, P. A. C., and Prather, R. S.: Effects of liquid-phase electrical conductivity water content and surface conductivity on bulk soil electrical conductivity, Soil Sci. Soc. Am. J., 40, 651–665, 1976.
Sander, T. and Gerke, H. H.: Preferential flow patterns in paddy fields using a dye tracer,

Vadose Zone. J., 6, 105–115, 2007.
Seibert, J. and McGlynn, B. L.: A new triangular multiple flow direction algorithm for computing upslope areas from gridded digital elevation models, Water Resour. Res., 43, W04501, doi:10.1029/2006WR005128, 2007
Schäuble, H., Marinoni, O., and Hinderer, M.: A GIS-based method to calculate flow accumulation by considering dams and their specific operation time, Comput. Geosci., 34, 635–646, 2008.
Sherlock, M. D. and McDonnell, J. J.: A new too for hillslope hydrologists: spatial distributed groundwater level and soilwater content measured using electromagnetic induction, Hydrol. Processes, 17, 1965–1977, 2003
Sidle, R. C., Noguchi, S., Tsuboyama, Y., and Laursen, K.: A conceptual model of preferential flow systems in forested hillslopes: evidence of self-organization, Hydrol. Processes, 15, 1675–1962, 2001.
Soil Survey Division Staff: Soil Survey Manual, U.S. Department of Agriculture Handbook No. 18, US Government Printing Office, Washington, D.C., USA, 1993.
Tarboton, D. G.: A new method for the determination of flow directions and upslope areas in grid digital elevation models, Water Resour. Res., 33, 309–319, 1997.
Thompson, J. A., Pena-Yewtukhiw, E. M., and Grove, J. H.: Soil-landscape modelling across a physiographic region: Topographic patterns and model transportability, Geoderma, 133, 57–70, 2006.
Tsukamoto Y. and Ohta, T.: Runoff process on a steep forested slope, J. Hydrol., 102, 165–178, 1988.
Vachaud, G., De Silans Passerat, A., Balabanis, P., and Vauclin, M.: Temporal stability of spatial measured soil water probability density function, Soil Sci. Soc. Am. J., 49, 822–827, 1985.
Van Genuchten, M. T.: A closed form equation for predicting the hydraulic conductivity of unsaturated soils, Soil Sci. Soc. Am. J., 44, 892–898, 1980.
Vogt, J. V., Colombo, R., and Bertolo, F.: Deriving drainage networks and catchment boundaries: a new methodology combining digital elevation data and environmental characteristics, Geomorphology, 53, 281–298, 2003.
Walker, C. and Lin, H. S.: Soil Property Changes after Four Decades of Wastewater Irrigation: A Landscape Perspective, Catena, 73, 63–74, 2008.
Wu, S., Li, J., and Huang, G. H.: A study on DEM-derived primary topographic attributes for hydrologic applications: sensitivity to elevation data resolution, Appl. Geogr., 28, 210–223,

2008.
Yaalon, D. H., Jungreis, C., and Koyumjisky, H.: Distribution and reorganization of manganese in three catenas of Mediterranean soils, Geoderma, 7, 71–78, 1972.
Zhu, Q. and Lin, H. S.: Interpolation of soil properties based on sample size, spatial structure, and auxiliary variable in two contrasting landscapes, Catena, in review, 2009.

Table 1. Distribution of the number of soil moisture monitoring sites and soil core descriptions at the Kepler Farm among different slope classes, depth to bedrock ranges, and soil series.

Variable categories		Soil moisture content monitoring sites	Soil matric potential monitoring sites	Soil cores described
Slope (%)	<3	23	11	10
	3~8	80	40	37
	>8	42	23	23
Depth to bedrock (m)	<0.5	34	17	15
	0.5~1.0	59	10	13
	>1.0	52	47	42
Soil series	Opequon	48	27	18
	Hagerstown	63	34	36
	Murrill	17	6	7
	Nolin	10	4	6
	Melvin	7	3	3
Total		145	74	70

HESSD
6, 2893–2929, 2009

HESSD

6, 2893–2929, 2009

Subsurface lateral flow paths in an agricultural landscape

Q. Zhu and H. S. Lin

Table 2. The time table of soil water content and matric potential data collections at the Kepler Farm in this study.

Year	2005	2006	2007	2008
Whole farm soil water content (145 sites)	17 May, 15 June, 10 and 18 July, 3 August, and 14 October	20 and 21 June	13 and 29 March, 20 April, and 15 May	None
Soil water content and matric potential (76 sites)	None	20, 21, and 30 June, 3 and 11 July	5 and 29 June, 15 July, 31 October	12, 19, and 26 June, 3 and 10 July

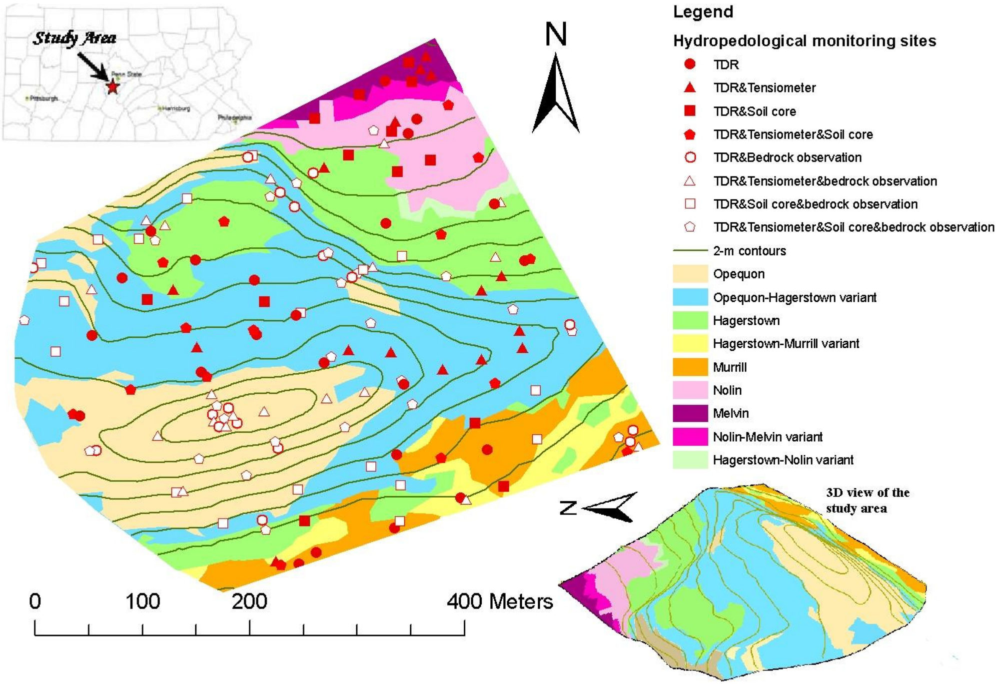

Fig. 1. The study area and the spatial distribution of monitoring/observation sites for soil moisture (TDR), matric potential (tensiometers), soil cores, and depth to bedrock (bedrock observation) at the Kepler Farm located in central Pennsylvania, USA.

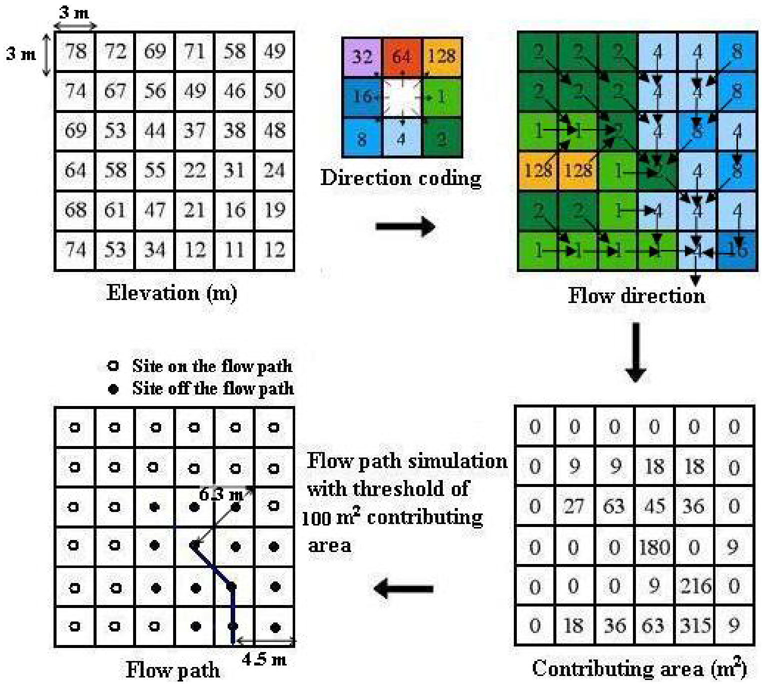

Fig. 2. An illustration of determining the flow path from the digital elevation model (DEM) using the deterministic 8 single-flow algorithm (D8). The "direction coding" shows the codes (i.e., 1, 2, 4, 8, 16, 32, 64, and 128) of the eight valid output directions into which flow could travel. The "flow direction" is determined by finding the direction of maximum drop from each cell through the DEM. The "contributing area" of a specific cell is determined by the number of cells draining into it and the cell size ($3\times3=9\,m^2$) of the DEM. The "flow path" is generated by setting the threshold of contributing area (e.g., $100\,m^2$ in the above illustration). If a soil water monitoring site is in a cell of the simulated flow path or adjacent to it, then it is considered as on the simulated flow path in this study.

HESSD
6, 2893–2929, 2009

Title Page
Abstract | Introduction
Conclusions | References
Tables | Figures
◂ | ▸
Back | Close
Full Screen / Esc
Printer-friendly Version
Interactive Discussion

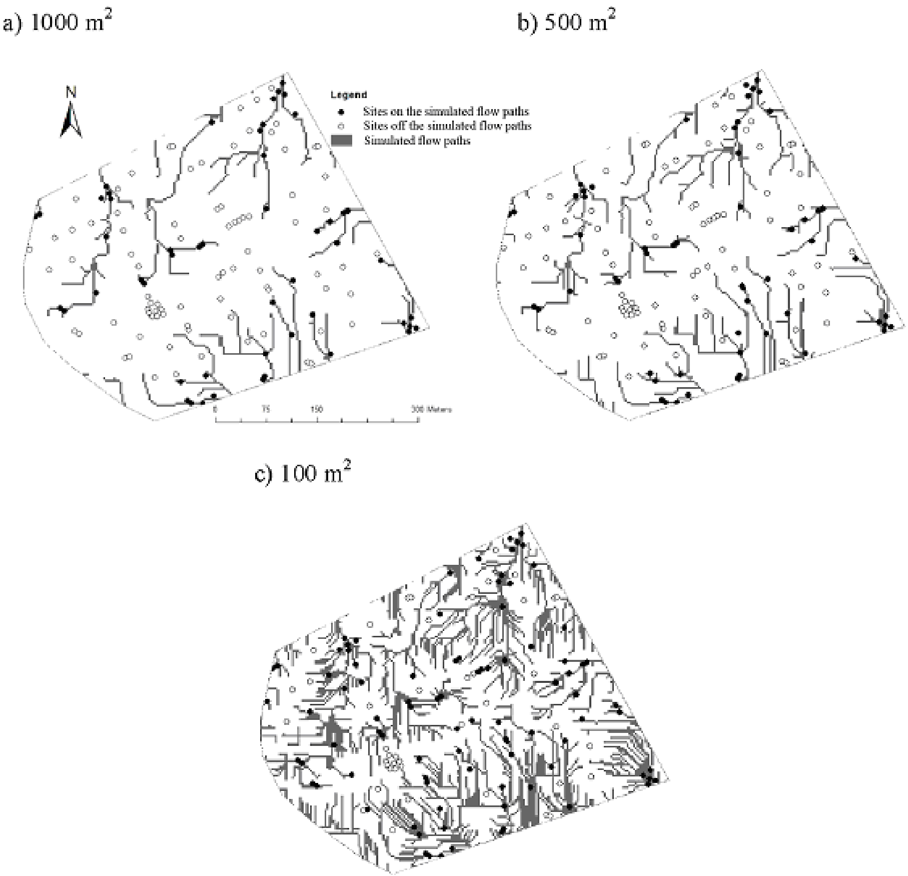

Fig. 3. Simulated flow paths at the soil-bedrock interface using three thresholds of contribution area: **(a)** 1000 m^2, **(b)** 500 m^2, and **(c)** 100 m^2. Simulated flow paths at the Ap1–Ap2 interface and the interface with the clay layer are similar to these shown here.

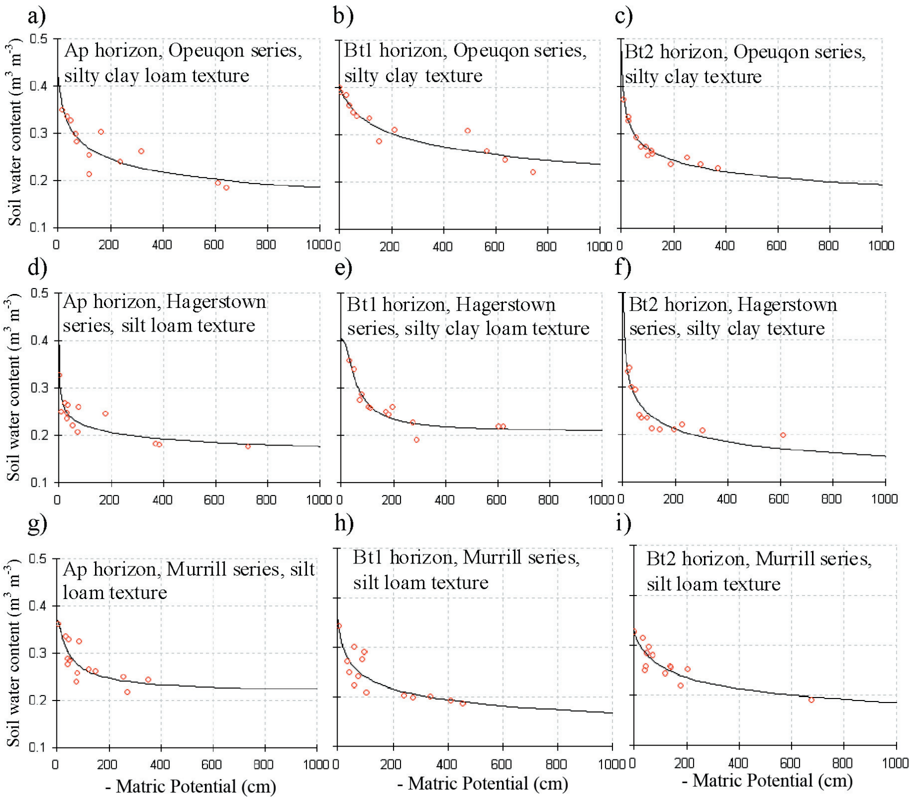

Fig. 4. Examples of fitted soil water retention curves for **(a)** Ap (silty clay loam), **(b)** Bt1 (silty clay), **(c)** Bt2 (silty clay) horizons at site 9 (the Opequon series), **(d)** Ap (silt loam), **(e)** Bt1 (silty clay loam), **(f)** Bt2 (silty clay) horizons at site 85 (the Hagerstown series), **(g)** Ap (silt loam), **(h)** Bt1 (silt loam), and **(i)** Bt2 (silt loam) horizons at site 65 (the Murrill series) using the parametric model of van Genuchten (1980).

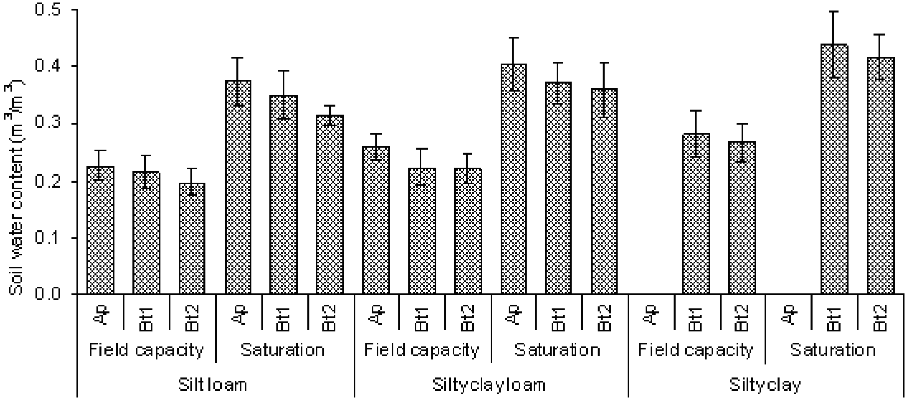

Fig. 5. Average volumetric soil water contents and their standard deviations at field capacity and saturation based on field observed soil water content and matrix potential for different textural classes and horizons at the Kepler Farm.

HESSD
6, 2893–2929, 2009

Subsurface lateral flow paths in an agricultural landscape

Q. Zhu and H. S. Lin

Title Page
Abstract Introduction
Conclusions References
Tables Figures
◀ ▶
Back Close
Full Screen / Esc
Printer-friendly Version
Interactive Discussion

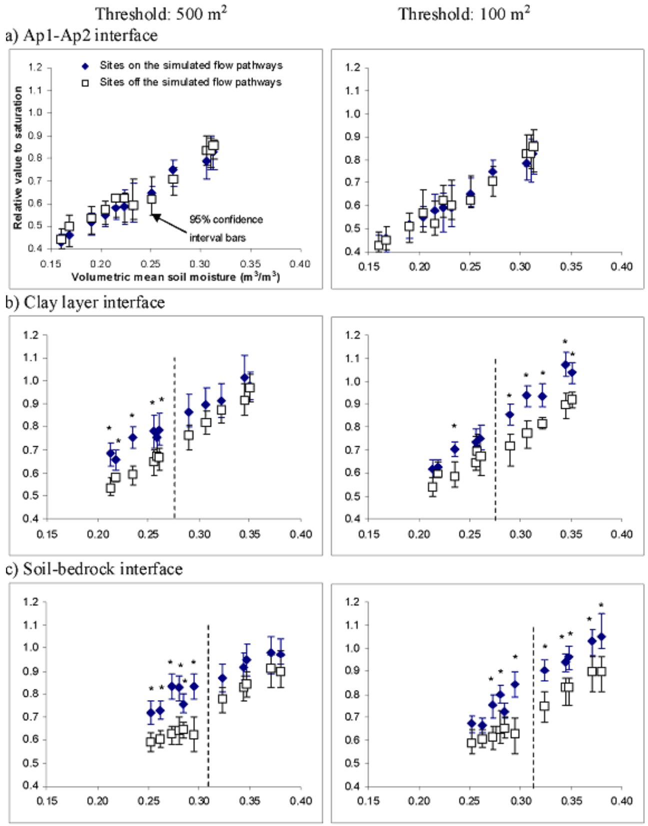

Fig. 6. Comparison of the means and 95% confidence intervals of relative saturation (*RS*) at monitoring sites on and off the simulated flow paths with thresholds 500 and 100 m^2 for **(a)** the Ap1–Ap2 interface, **(b)** the clay layer interface, and **(c)** the soil-bedrock interface. Dash lines separate the relatively dry and wet conditions. Bars labeled with asteroid (*) indicate statistically significant difference at $p<0.05$ level between sites on and off the simulated paths.

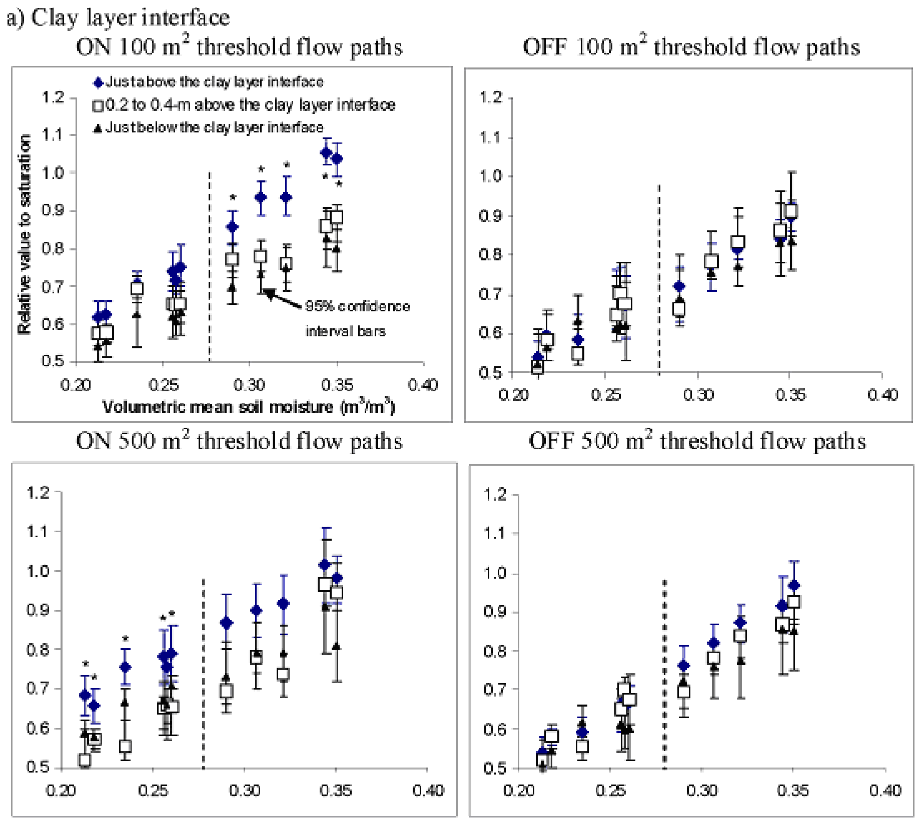

Fig. 7a. Comparison of the means and 95% confidence intervals of the relative saturation (*RS*) at the monitoring sites on and off the simulated flow paths with thresholds of 500 and 100 m^2 for **(a)** the interface with the clay layer and **(b)** the interface with the bedrock. Within each graph, the comparison is for *RS* just above or below the specified interface and 0.2 m above the interface. Dash lines separate the relatively dry and wet conditions. Bars labeled with asteroid (*) indicate statistically significant difference at $p<0.05$ level.

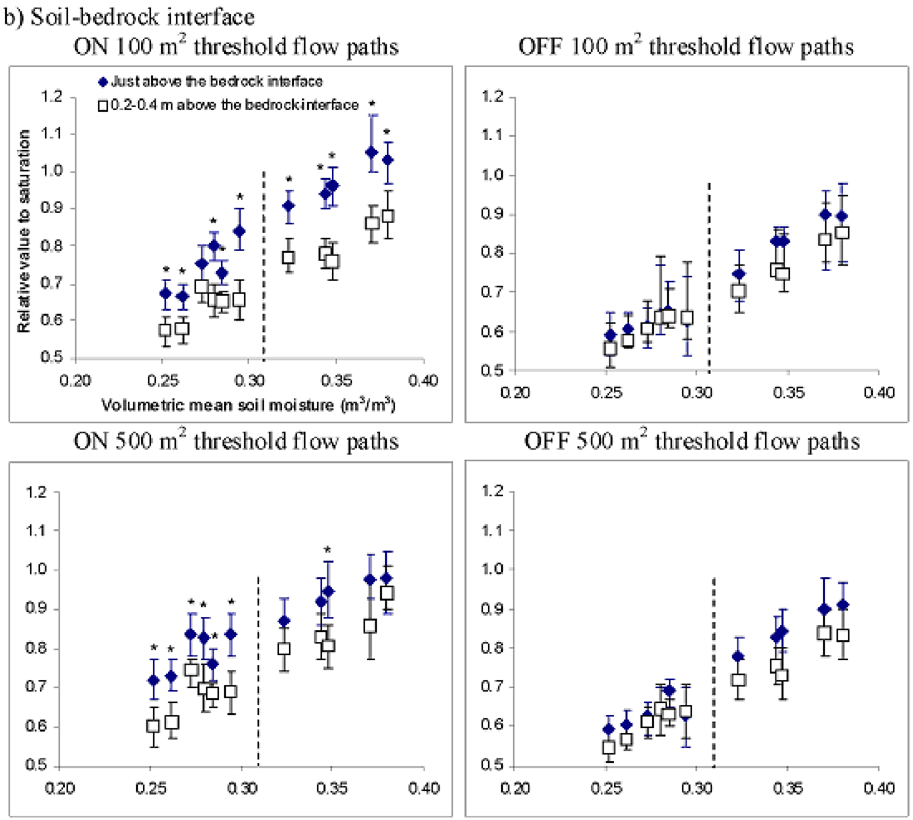

Fig. 7b. Continued.

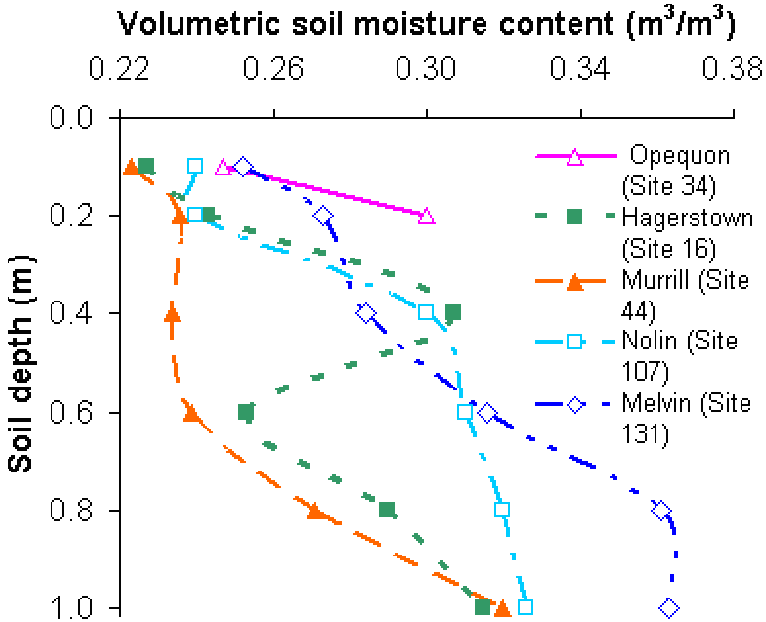

Fig. 8. Typical profile distribution of volumetric soil water content in each of the five soil series identified in the study area (i.e., the Opequon, Hagerstown, Murrill, Nolin, and Melvin series).

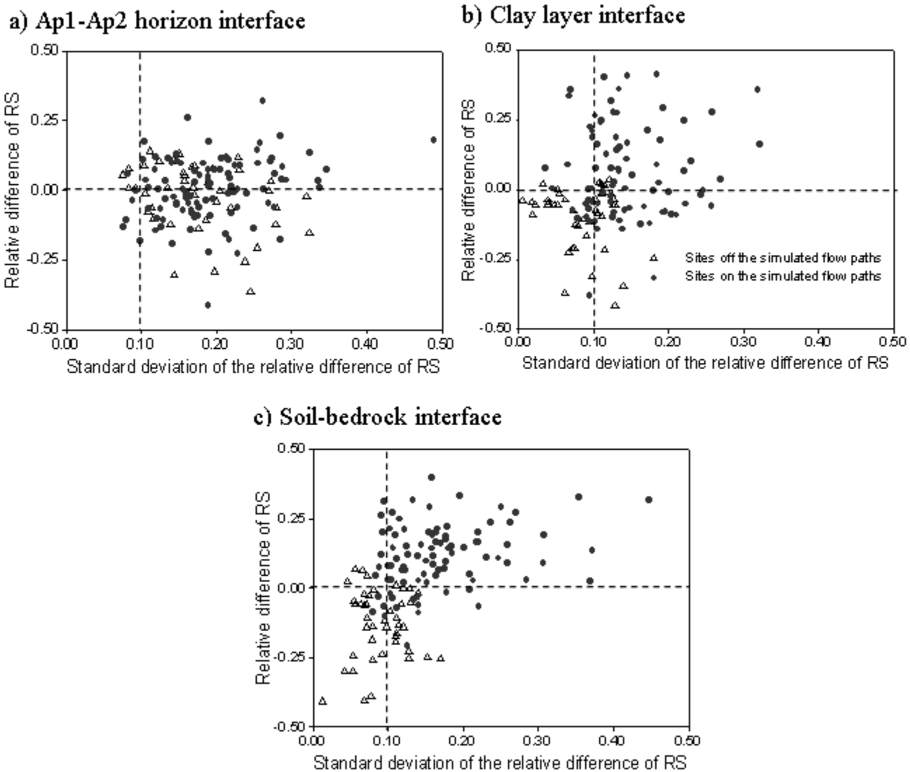

Fig. 9. Temporal stability of relative saturation (*RS*) at the monitoring sites on and off the simulated flow paths (using the threshold of 100 m^2) at **(a)** the Ap1–Ap2 interface, **(b)** the clay layer interface, and **(c)** the soil-bedrock interface. Sites with positive relative difference were wetter than the overall mean of the entire farm. Sites with high standard deviations of the relative difference were temporally unstable.

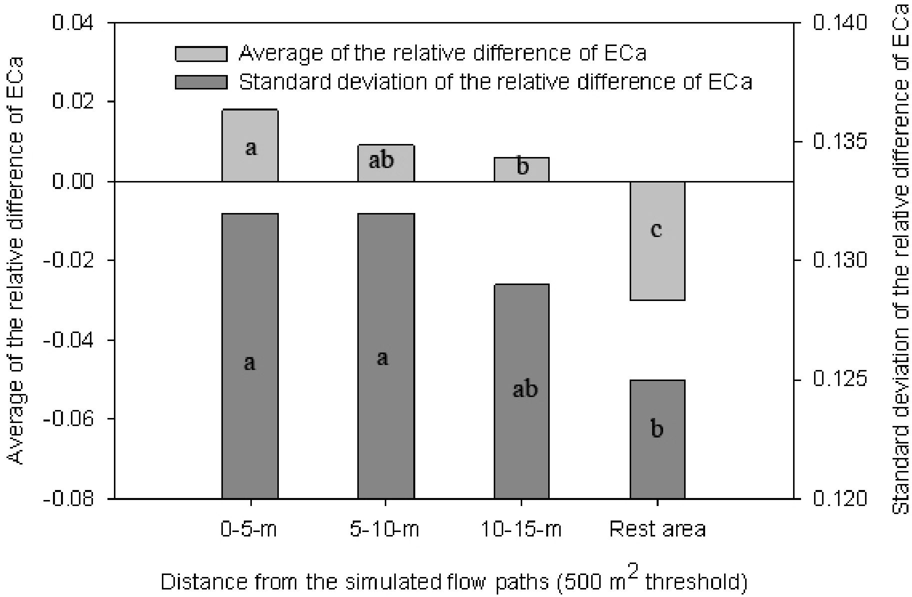

Fig. 10. Temporal stability of apparent electrical conductivity (ECa) in areas with different distances away from the simulated flow paths (using the threshold of 500 m^2). Areas with positive relative difference in ECa indicate a higher ECa value than the overall mean of the study area. Areas with high standard deviations of the relative difference in ECa indicated temporally more dynamics (or unstable). Bars with the same letter are not statistically significantly different from each other at p<0.05 level.

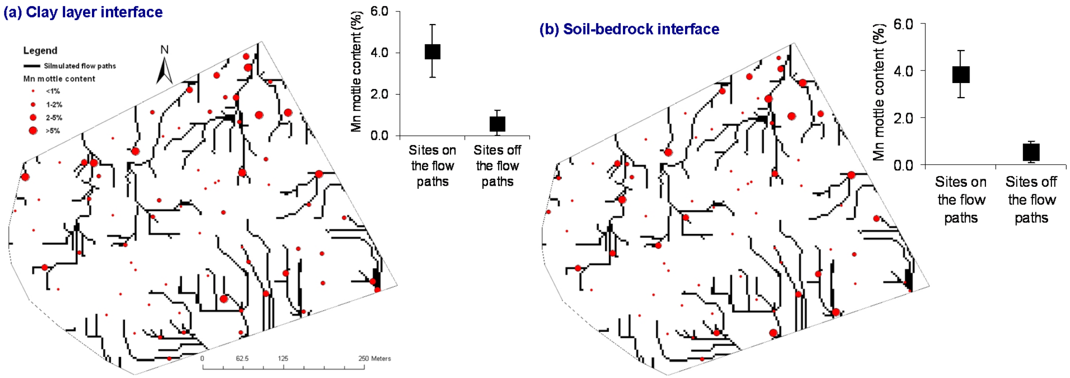

Fig. 11. Observed Mn contents in the soil profiles at **(a)** the clay layer interface and **(b)** the soil-bedrock interface in relation to the simulated flow paths (using a threshold of 500 m^2). In the insets, Mn contents on and off the simulated flow paths are compared. Bars with different letters are statistically significantly different at $p<0.05$ level.